

Mechanical and Electrochemical Implications of Drying Temperature on Lithium-Ion Battery Electrodes

Alexander Kukay,^[a, b] Georgios Polizos,^[b] Emily Bott,^[a, b] Anton Ielhev,^[c] Runming Tao,^[b] Jaswinder Sharma,^[b] and Jianlin Li^{*[d]}

Lithium-ion battery (LIB) electrodes are typically produced with n-methyl-2-pyrrolidone, a toxic solvent that is a known carcinogen and reproductive hazard. Accordingly, aqueous processing has been an expanding area of research interest in the field of LIB manufacturing. Although aqueous processing has been widely successful in anode processing, serious challenges remain in processing the cathode. In this work, the drying mechanics of cathode processed with both solvents is investigated through implementation of a chemical-engineering-based model to better understand the utilization of heat provided by experimentally determining the heat and mass transfer coefficients. Electrochemical performance is also eval-

uated to determine the impact of drying temperature on cycling performance. Binder distribution is determined via various methods to confirm differences in binder homogeneity as a function of both solvent and drying temperature. Identified is the large difference in the efficiency in which the heat is used as well as an ideal drying temperature for both aqueous and non-aqueous processed cathodes. Also identified is the increased sensitivity to processing temperature for aqueous processed electrodes compared to non-aqueous processed counterparts, pointing to the possibility of tuned drying regimes which would capitalize on the potential cost savings of aqueous processing for cathodes.

This manuscript has been authored in part by UT-Battelle, LLC, under contract DE-AC05-00OR22725 with the US Department of Energy (DOE). The US government retains and the publisher, by accepting the article for publication, acknowledges that the US government retains a nonexclusive, paid-up, irrevocable, worldwide license to publish or reproduce the published form of this manuscript, or allow others to do so, for US government purposes. DOE will provide public access to these results of federally sponsored research in accordance with the DOE Public Access Plan (<http://energy.gov/downloads/doe-public-access-plan>).

Introduction

Lithium-ion batteries (LIBs) are essential for energy storage in many fields.^[1] Although many processing and materials improvements have been implemented since the market adoption of conventional LIBs,^[2] electrode drying and the associated physics of particles, are still far from optimized.^[3] It has been demonstrated that electrode drying is the most energy intensive step, accounting for more than 46% of energy consumption during the LIB manufacturing process.^[4] Although the overall environmental impact of LIBs replacing internal combustion engines (ICEs) having become obvious over the past few decades, less discussed is the environmental impact of producing LIBs. The environmental and ethical considerations around production of LIBs should be paramount as the production of these materials continues to scale. Judicious choice of both material and methods with the goal of minimizing environmental impact should be prioritized so long as electrochemical performance, mechanical integrity, and operational safety are not compromised. Research has shown global warming potential associated with production of LIBs and has identified solvent replacement in both the cathode and anode as a promising avenue for improving the total environmental impact of LIBs during both production and use phase.^[5] The common organic solvent of choice for LIBs, n-methyl-2-pyrrolidone (NMP), is toxic, expensive, and restricted from use in some countries, making it a good candidate for replacement for both environmental and economic reasons.^[6] As cathode manufacturing has been identified as a disproportionately large contributor to overall environmental impact of LIB production, this work focuses on optimization of manufacturing cathodes, specifically energy input during the energy intensive drying period.^[7]

[a] Dr. A. Kukay, E. Bott
Bredesen Center for Interdisciplinary Research and Graduate Education,
University of Tennessee, Knoxville, Tennessee 37996, USA

[b] Dr. A. Kukay, Dr. G. Polizos, E. Bott, Dr. R. Tao, Dr. J. Sharma
Electrification and Energy Infrastructures Division, Oak Ridge National
Laboratory, Oak Ridge, Tennessee, 37830, USA

[c] Dr. A. Ielhev
Center for Nanophase Materials Sciences, Oak Ridge National Laboratory,
Oak Ridge, Tennessee, 37830, USA

[d] Dr. J. Li
Applied Materials Division, Argonne National Laboratory, Lemont, IL 60439,
USA
E-mail: jianlin.li@anl.gov

 © 2024 The Authors. Batteries & Supercaps published by Wiley-VCH GmbH. This is an open access article under the terms of the Creative Commons Attribution Non-Commercial License, which permits use, distribution and reproduction in any medium, provided the original work is properly cited and is not used for commercial purposes.

Electrode drying poses a technically difficult endeavor due to the complexity of measuring dynamic particle motion as well as the existence of a wide range of length scales participating in the diffusive and convective motion. These length scales range from nanometers when considering particle interactions and surface charge to hundreds of microns when considering ultra-thick electrodes and the distance solvent must travel from the current collector to the electrode surface during drying. Practically this requires physical models that account for a large variety of interactions.^[8] Regardless of the difficulty associated with measuring particle motion, the drying phase of electrode processing has a large impact on final performance and should be the subject of increased investigation.^[9] During the particulate coating drying process, three main forces must be considered. First, the evaporation of the solvent from the sample surface drives a consolidation front and results in a continual reduction in film thickness. Secondly, thermal Brownian diffusion of the particles results in randomly distributed particles and counteracts potential concentration gradients. Third, sedimentation effects are observed when the density of the particulate exceeds that of the solvent, resulting in the eventual basis of the porous electrode network. The combination of all three of these forces heavily influence the resulting porous network in particulate coatings, such as porous electrodes used in LIBs and can be visualized in Figure 1, only active material particles are shown in this diagram for simplicity but carbon based conductive additive particles and polymer binder particles are also present at a much smaller scale.^[10] These different forces and the effects on downline electrode processing has made electrode drying an area of significant interest in the field of battery production.

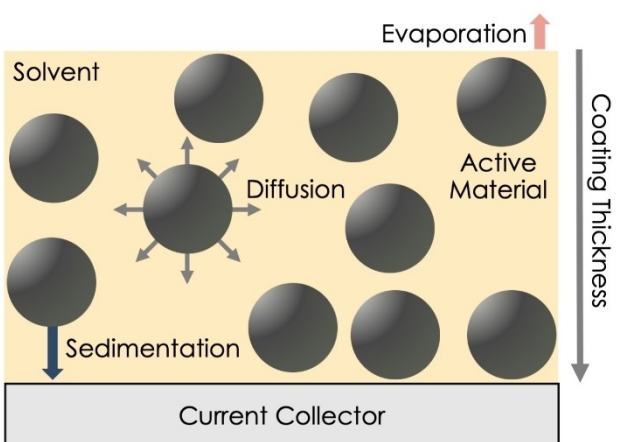


Figure 1. Film shrinkage stage of electrode drying. Diffusion driven by Brownian motion is represented by multi-directional arrows showing potential for multi-directional movement based on concentration gradients and thermal forces. Sedimentation is represented by a dark blue arrow and shows the effect of gravity acting on the active material particle. Evaporation is shown as an upward arrow depicting the direction of vaporized solvent motion. As the solvent evaporates, the coating continually shrinks, as shown by the side arrow depicting coating thickness. Not shown in this graphic are the conductive additive and polymer binder particles for simplicity. These unshown particles are also affected by the combination of the previously mentioned forces.

Throughout the electrode production process, great care is taken to ensure homogenous distribution of material within the dispersion.^[9c] There is a wealth of research concerning optimization of the mixing processes available in literature and the impact of mixing sequences, conditions, times, and techniques on final dispersion behavior.^[11] As the importance of a well distributed combination of active material, conductive additive, and polymer binder is clear, a detailed understanding of how the distribution of these materials varies as the solvent is removed is paramount. During these processes, solvent is a critical factor as the viscosity and evaporation behavior dominate the redistribution of materials within the electrode during drying.^[9c] Considering the large electrode coating area, LIB electrodes can be accurately treated as thin films with two main drying phases.^[9c,12] First the solvent evaporation results in larger particles compacting and forming the basis of the electrode structure, commonly referred to as *film shrinkage*. Consolidation continues until the larger active material particles can no longer be compacted by evaporation of solvent. The drying behavior is then more accurately described by a *pore emptying* stage where excess solvent is removed from the previously formed porous electrode. This second stage comprises the bulk of time and energy input during drying. Smaller conductive additive and polymer binder particles still experience significant mobility at this stage as there is still sufficient solvent in the electrode system to transport these particles. These smaller particles experience transport through the initial electrode structure via Brownian motion due to the thermal energy of the electrode system as well as capillary action driven by the evaporation at the electrode surface. The transport of binder polymer chains dissolved in solution via diffusion is greater during the initial stage of drying than it is during the final, longer stage of pore emptying.^[9a,12–13]

Along with the mechanical implications of drying parameters, there also exist economic drivers to optimize the drying time and energy input. As the production phase of LIBs accounts for the majority of the overall cost of production and almost half of that cost results from drying and solvent capture related processes.^[14] By optimizing the time and energy required for drying, both capital and energy costs may be decreased, resulting in a more cost-effective processing technique and ultimately a more affordable battery. As the typical solvent, NMP, and prospective replacement solvent, deionized water (DI) have considerably different vapor pressures, 1.0 mm Hg at 40 °C compared to 55.3 mm Hg at 40 °C, and boiling points 204.3 °C and 100 °C respectively, the energy required as well as the rate of evaporation during electrode drying vary widely.^[15] NMP does however have a lower heat of vaporization than water, 510 kJ/kg, as opposed to 2260 kJ/kg for water, posing an economic advantage in the form of energy input required for NMP use. This slight advantage toward NMP is quickly negated when the toxic nature and legal limitations of NMP begin to be factored in as they account for a significant cost addition.^[16] Solvent replacement for anode chemistries, typically composed of graphite, has seen commercial success and is common in current manufacturing methods. Cathode chemistries have not enjoyed the same level of success, largely

due to a proton exchange reaction driven by lithium leaching from the active material particles into solution which leads to a highly basic environment.^[17] There is an abundance of research activity surrounding aqueous processing of cathode materials, but there are still considerable barriers to be overcome.^[18]

There have been numerous studies addressing drying parameters, mainly in conventionally processed (NMP processed) anodes.^[19,20] However, there is little information concerning cathode drying, especially as a function of solvent available in the literature. Previous investigations have detailed techniques for determining binder distribution as a function of drying condition and provided some insight on the electrochemical performance differences that are associated with high and low drying rates.^[6b,9c,21–24]

This work aims to expand on the current understanding of drying mechanics in LIB cathodes as well as investigates the effects of solvent replacement on drying rate along with binder distribution throughout the electrode. Results from this work will inform the future processing and manufacturing of LIB cathodes and provide further understanding on the advantages and limitations of aqueous processing of cathode materials.

Experimental Section

Electrode preparation: Small scale dispersions were prepared by adding components in steps and mixing thoroughly using a high shear mixer (NETZSCH Premier Technologies Model 50). Before adding additional material, the slurry was checked to ensure homogenous distribution of materials to reduce the possibility of agglomerates. Sample compositions were limited to two formulations, one utilizing DI water (purified to 18 MΩ cm using a Milli-Q Direct 8 purifier) and the other using the conventional NMP (Sigma Aldrich) as the solvent. Each dispersion had a solids composition of 90 wt.% active material (NMC 811, Targray 12 µm D₅₀), 5 wt.% conductive additive (carbon black, Denka Li-100) and 5 wt.% binder. Binder selection was dependent on solvent. Aqueous processing utilized a composite binder consisting of a 0.5 wt.% phosphoric acid and a 1:4 mass ratio of sodium substituted carboxymethyl-cellulose salt (Arcos Organics, MW: 250,000, DS: 0.9) and emulsion

binder (JSR TRD-202 A) whereas NMP processed samples used PVDF (5130, Solvay) as the binding agent. Phosphoric acid was added in the aqueous slurries only to neutralize the pH of the slurry and mitigate the corrosion of the aluminum current collector.^[17b] NMP-based electrodes were prepared with 48 wt.% solids content and DI based samples were prepared with 52 wt.% solids content to adhere to practical solids content conditions observed in production. Samples were placed on a rolling mill between tests to avoid sedimentation. A test matrix of coating thickness and drying temperatures can be found in Table 1.

Drying curve acquisition: Prepared slurries were coated on aluminum foil cut to 7.62 cm×12.70 cm (3 in×5 in) areas using a doctor blade with a wet gap of either 400 or 750 µm to obtain electrodes with areal loading of 2.5 or 6 mAh cm⁻², and thickness of 80 or 150 µm, respectively. The entire area was coated to ensure a constant surface area for modeling the heat transfer to the electrode. The resulting coatings were then placed on a weighing platform suspended from a precision balance (Mettler Toledo) for real time mass collection. A forced air heater as well as a heated bed were used in tandem to control the temperature of the sample space throughout the test. This setup was designed to emulate a typical forced-air drying condition that would be present in a slot-die coater. A schematic of this experimental setup is provided in Figure 2. Three test temperatures were used, 60 °C, 90 °C, and 125 °C. Air flow was limited to 10 cubic feet per minute to reduce the variance in the mass reading due to turbulent air. A Python script was developed to communicate with the balance on one second intervals, recording the mass with each interval. A thermocouple was used to measure the film temperature of each sample during testing. A duplicate film was coated and placed near the weighing platform and the temperature of the second film was measured as to not influence the mass measurements of the primary film. Temperature measurements were collected every second for the duration of the drying period.

Heat and mass transfer coefficient model: Heat and mass transfer coefficients were calculated using a model developed based on chemical engineering principles.^[25] First the mass transfer coefficient is calculated using the following equation.

$$M(t) = M_0 - K_g \bullet A \bullet t \bullet (P_V(T) - P_0) \quad (1)$$

Table 1. Heat Transfer Coefficient and Total Heat Transfer Rate values for each composition.

| Solvent | Drying Temperature (°C) | Coating Wet Gap (µm) | Heat Transfer Coefficient, H_c (W/m ² K) | Mass Transfer Coefficient, K_g (g cm ⁻² s ⁻¹ bar ⁻¹) | Mass Transfer Coefficient, K_c (cm/s) | Total Heat Transfer Rate, $-q$ (W) | Rate of Vaporization, \dot{m} (mg/s) |
|---------|-------------------------|----------------------|---|--|---|------------------------------------|--|
| DI | 60 | 400 | 115.1 | 7.10E-03 | 10.0 | 30.6 | 13.5 |
| DI | 60 | 750 | 118.7 | 7.30E-03 | 10.4 | 30.2 | 13.4 |
| DI | 90 | 400 | 155.8 | 9.40E-03 | 13.6 | 73.5 | 32.5 |
| DI | 90 | 750 | 168.6 | 1.02E-02 | 14.7 | 80.8 | 35.8 |
| DI | 125 | 400 | 183.3 | 1.07E-02 | 16.0 | 133.3 | 59.0 |
| DI | 125 | 750 | 215.5 | 1.27E-02 | 18.8 | 159.3 | 70.5 |
| NMP | 60 | 400 | 3.5 | 1.20E-03 | 0.3 | 0.6 | 1.2 |
| NMP | 60 | 750 | 2.6 | 9.00E-04 | 0.2 | 0.5 | 1.0 |
| NMP | 90 | 400 | 5.7 | 1.90E-03 | 0.5 | 2.1 | 4.1 |
| NMP | 90 | 750 | 5.4 | 1.80E-03 | 0.5 | 2.0 | 3.9 |
| NMP | 125 | 400 | 6.1 | 2.00E-03 | 0.6 | 3.4 | 6.7 |
| NMP | 125 | 750 | 5.9 | 1.90E-03 | 0.5 | 3.3 | 6.5 |

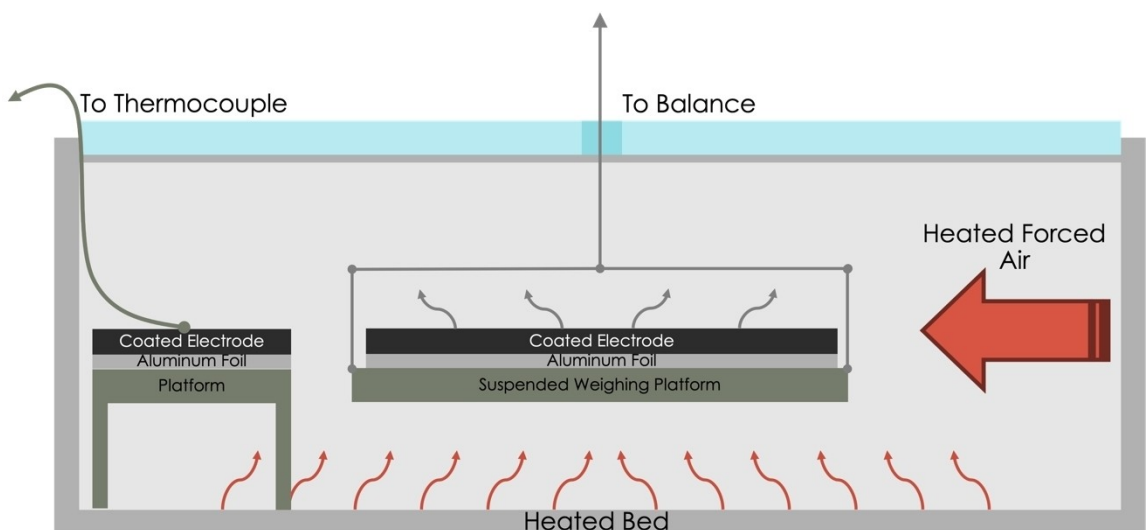


Figure 2. A schematic of the real time mass acquisition during both phases of electrode drying. A forced air heater and bed heater are used to control the ambient temperature in the tape caster and provide a uniform distribution of heat throughout the sample space. The air flow was fixed at 10 cubic feet per minute to reduce variance from turbulent air. Both changes in mass and temperature were recorded as a function of time via a laboratory balance and thermocouple.

Where $M(t)$ is the measured mass as a function of time, M_0 is the initial mass value, K_g represents the mass transfer coefficient, A is the effective area of the sample (assumed to be the solids volume fraction multiplied by the geometric sample area), t is time, $P_V(T)$ is the solvent vapor pressure calculated using Antoine equation, and P_0 is the partial pressure of the solvent in air.

Along with a mass-based mass transfer coefficient, a concentration-based mass transfer coefficient calculation was also used, implementing the Chilton-Colburn J-Factor analogy. This is given by Equation 2,

$$K_g \bullet P_V(T) = \frac{K_c \bullet P_V(T)}{R_{Solvent} \bullet T} \quad (2)$$

Where, K_c is the concentration based mass transfer coefficient, $R_{Solvent}$ is the mass specific gas constant for the solvent used and the concentration of solvent vapor follows the model of an ideal gas mixture presented in Equation 3.

$$\frac{m}{V} = \frac{P_V(T)}{R_{Solvent} \bullet T} \quad (3)$$

The concentration based heat transfer coefficient, H_c , can then be calculated by utilizing the Chilton-Colburn J-Factor analogy shown in Equation 4,^[26]

$$H_c = K_c \bullet \rho_{air} \bullet C_{p,air} \bullet \left(\frac{Sc}{Pr} \right)^{\frac{2}{3}} \quad (4)$$

where, H_c is the heat transfer coefficient, $C_{p,air}$ is the constant pressure of heat capacity for air, Sc is the Schmidt number, and Pr is the Prandtl number and are calculated via Equation 5,

$$\frac{Sc}{Pr} = \frac{k}{\rho_{air} C_{p,air} D_{AB}} \quad (5)$$

where, k is the thermal conductivity of air and D_{AB} is the diffusivity of a volatile species in air. The value of D_{AB} for NMP in air is an order of magnitude estimation and assumes low concentration of NMP in air. In other words, sufficient air flow must be present to satisfy the bounds of the model.

This model was applied to all sample masses after collection within the first 500 seconds of drying as to capture the film shrinkage stage of drying only. The model was developed to capture the behavior of the electrode during the film shrinkage stage of drying and therefore is only acceptable to apply to timeframe with a linear reduction of mass as a function of time.

Binder distribution via time-of-flight secondary ion mass spectrometry (ToF-SIMS): Epoxy mounted cross-sectional samples were also used for ToF-SIMMS (IONTOF) analysis. Samples were first mounted in a two-part epoxy before grinding and polishing the surface to a 3000 grit finish. Samples were then analyzed with a 500 μm window and various dwell times to ensure sufficient signal. Binder content was ascribed to the positive cesium fluorine as both PVDF as well as the JSR acrylate binder contain fluorine. Cesium was the sputtering ion and readily reacts with the present fluorine to form Cs₂F⁺, which was used as opposed to the F⁻ ion signal to reduce the overall test time by only positive ion detection.

Cell Assembly and electrochemical testing: After drying the electrodes were calendered to ~30% porosity followed by an overnight drying at 110°C in a vacuum oven to remove any residual moisture from the electrode. Half cells (coin cells 2032) were then assembled in an argon filled glovebox with lithium metal counter electrodes, Celgard 2325 separator and Gen II electrolyte (1.2 M LiPF₆ dissolved in ethylene carbonate (EC) and ethyl methyl carbonate (EMC) in a 3:7 weight ratio). Charge/discharge tests were performed at constant current constant voltage (CC-CV) charge at various current rates (1 C = 190 mAh/g in a voltage range of 4.3–3.0 V on a Maccor cycler.

Results and Discussion

Heat and Mass Transfer Coefficient

The mass of each electrode normalized to the first data point is shown as a function of time in Figure 3 for each configuration and temperature. The data shown is only the coating mass as the balance was tared to the current collector mass before coating the slurry. Listed temperatures are the measured film temperature (T_s) and were used as the input of the model described previously. The data is shown as relative mass for presentation purposes and to compare the drying rates among samples, however the rate of change of the mass before normalization was used to calculate the heat and mass transfer coefficients. This was accomplished by taking the numerical first derivative of each data set with a moving window size of 50 points. Care was taken to only use the linear portion of the drying data and accordingly a cutoff of 500 seconds was used for each sample for consistency. The DI samples show much faster mass loss as compared to the NMP based electrodes during the first 500 seconds of drying at all temperatures. As the set temperature increased, the rate of mass loss for all samples increased, regardless of solvent. The differences in rate of mass loss were most apparent in the 750 μm wet gap DI based samples, which is expected as there is more solvent in the electrode and thus more solvent per unit time is expected

to be removed as the temperature increases. Figure 3 also indicates that the temperature sensitivity for each solvent is different. The DI samples span a range of 18°C (from 32.6°C to 50.0°C), whereas NMP based samples span 27°C (41.4°C to 68.0°C). The larger increase in film temperature for NMP samples as compared to DI samples while maintaining a lower evaporation rate is easily explained by the sizeable difference in the heat of vaporization between the two materials. Calculated values are listed in Table 1 and shown graphically in Figure 4.

The faster drying rate inferred by the data in Figure 3 is further explored by calculating the heat and mass transfer coefficients for each electrode and these values are shown in Figure 4. By keeping the coating areas constant, a direct comparison of the drying behavior as a function of area can be made. As the temperature is increased the heat and mass transfer coefficients for DI based electrodes increase monotonically, reaching their maximum at the highest set temperature (125°C) for both coating thicknesses. The NMP samples also exhibit increases to both the heat and mass transfer coefficients, however the increase is not monotonic and increases only slightly from 90°C to 125°C, suggesting diminishing returns as the temperature is increased further. Furthermore, the calculated mass transfer coefficients for the DI based electrodes are an entire order of magnitude greater than the NMP based electrodes across all temperatures. This suggests the DI samples utilize the applied heat more efficiently as

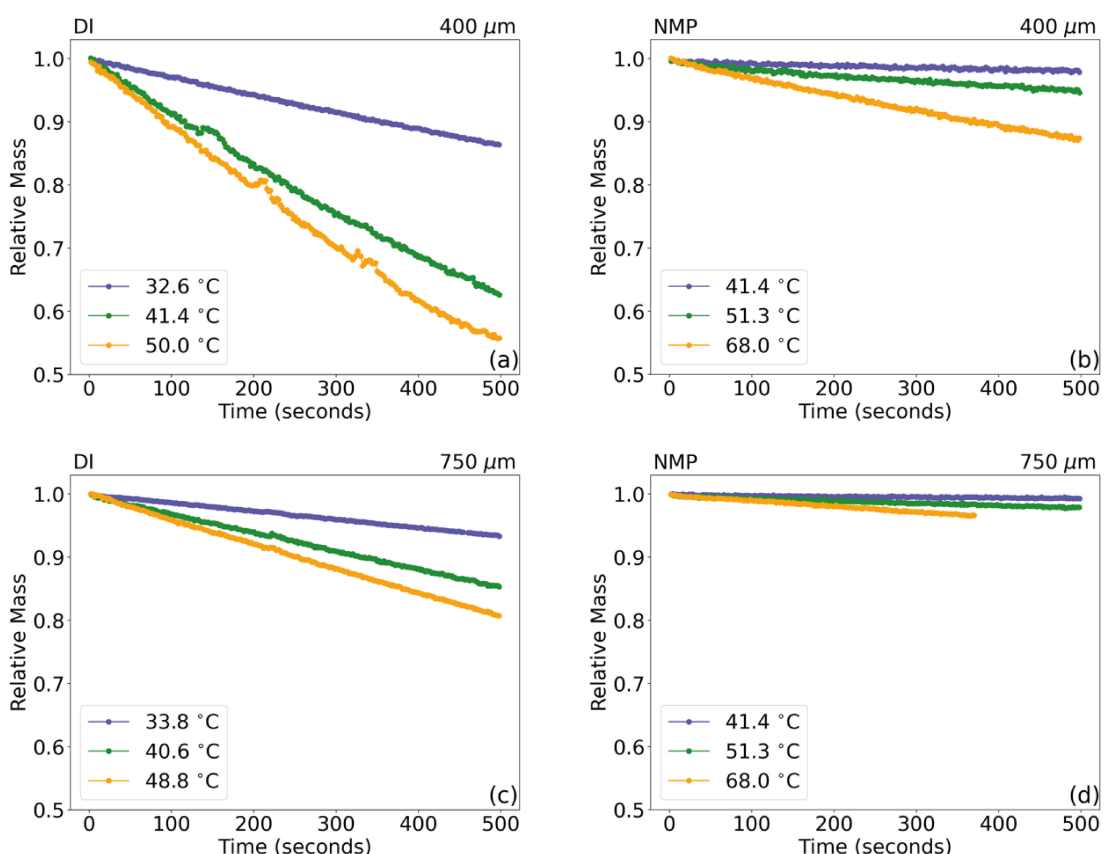


Figure 3. Experimentally measured mass time curves for a) DI 400 μm wet gap, b) NMP 400 μm wet gap, c) DI 750 μm wet gap, and d) NMP 750 μm wet gap. DI based samples exhibit much greater response to change in temperature as compared to the respective NMP sample.

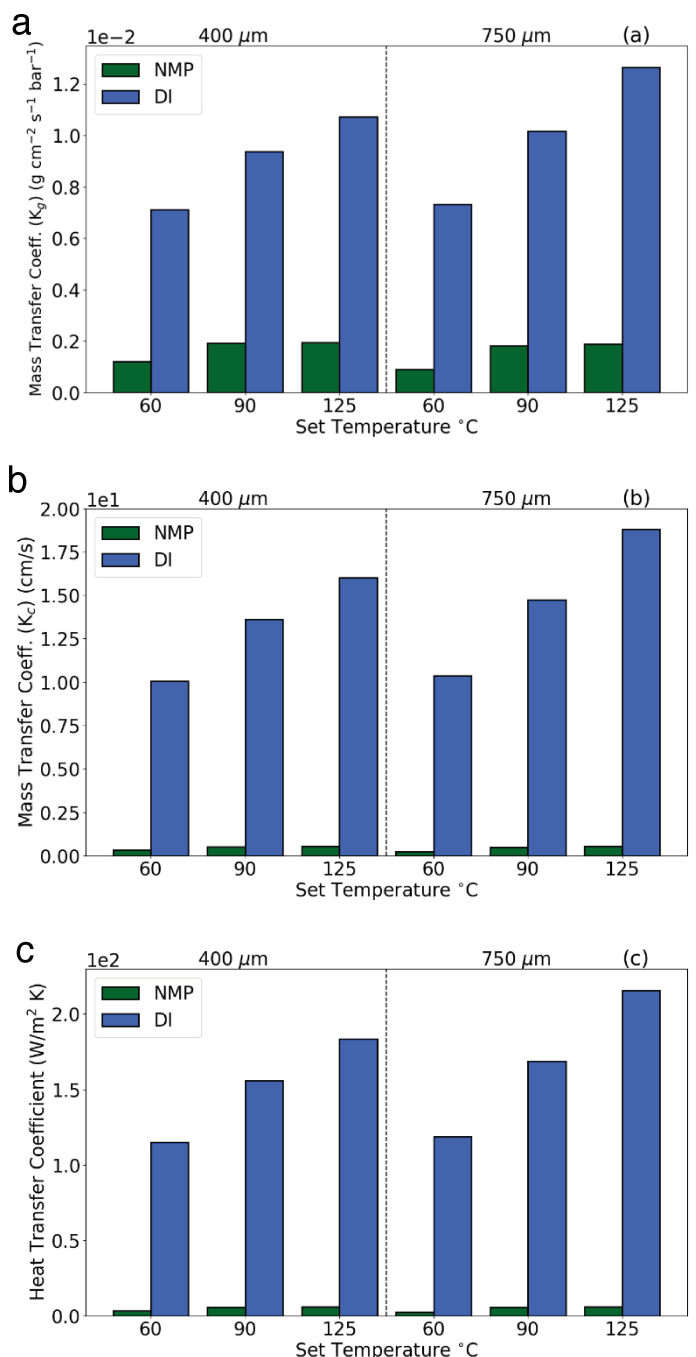


Figure 4. Calculated mass-based mass transfer coefficients (K_g) for a) NMP and b) DI based samples as well as concentration-based mass transfer coefficients (K_c) for c) NMP and d) DI based samples. Heat transfer coefficients (H_c) are given for e) NMP and f) DI samples.

compared to the NMP samples. The difference in heat transfer coefficients is greater yet at two orders of magnitude larger from NMP to DI across all samples.

To further explore the relationship of drying temperature to the drying efficiency of each electrode the total heat transfer rate per unit area (q) in terms of Joules per second was determined via Equation 6 where T_s is the measured film temperature, T_∞ is the temperature of the surround air, H_c is the calculated heat transfer coefficient and dA_s represent the

infinitesimal unit area. As the area used was constant across samples this simplifies to Equation 7 where A_s is now the nominal surface area of the electrode.^[25] Here a negative sign is introduced to reflect the physical nature of the phenomenon. In this scenario it is beneficial to have a positive value for the total heat transfer rate and thus reflect the total heat transferred to the electrode during the drying process in terms of Joules per second. The convention is introduced for clarity.

$$q = (T_s - T_\infty) \int_{A_s} H_c \cdot dA_s \quad (6)$$

$$-q = -(T_s - T_\infty) \cdot H_c \cdot A_s \quad (7)$$

The total heat transfer rate is shown in Figure 5 and illustrates the energy input as a function of time for each sample. A higher heat transfer rate suggests a more efficient use of the energy input into the system, providing further support for the argument that DI as a solvent uses the heat supplied more efficiently than NMP. Not only is the total heat transfer rate two orders of magnitude greater for DI samples as compared to NMP, the increase from each temperature is more significant. This is most clear when comparing set temperatures of 90 °C and 125 °C. The total heat transfer rate for the NMP samples increases from 2.0 W to 3.3 W, a 60% increase. The percent increase for the corresponding DI samples was from 80.8 W to 159.3 W, a near 100% increase. This provides further support for the increased sensitivity to processing temperature for DI based samples and if exploited correctly, can be used to reduce the overall energy input during electrode drying, one of the most energy intensive manufacturing steps a result that aligns nicely with previous modeling results.^[27]

Although values for the heat transfer rate illustrate the efficiency of the drying process for each solvent, going one step further and dividing the total heat transfer rate by the enthalpy of vaporization, $E_{vap.}$, for each material, provides the rate of evaporation (\dot{m}) in terms of milligrams per second via Equation 8. This value, while considering an ideal vaporization condition, demonstrates a ~10x increase in drying rate for DI samples over their NMP based counterparts and again illustrates a much greater increase between set temperature for DI based samples as compared to NMP samples as shown in Figure 5. This result provides a concrete number associated with solvent removal that can readily be applied to inline manufacturing. Since the solvent mass before drying is a readily available quantity, one would be able to estimate the total time required to dry an electrode and be able to optimize the manufacturing process accordingly.

Equation 8:

$$\dot{m} = \frac{-q}{E_{vap.}}$$

Combine the increased drying rate attained in the film shrinkage stage of drying with the ability to increase the solids loading from ~45% for NMP to upwards of 60% for DI water, the total time and energy dedicated to drying the electrode can

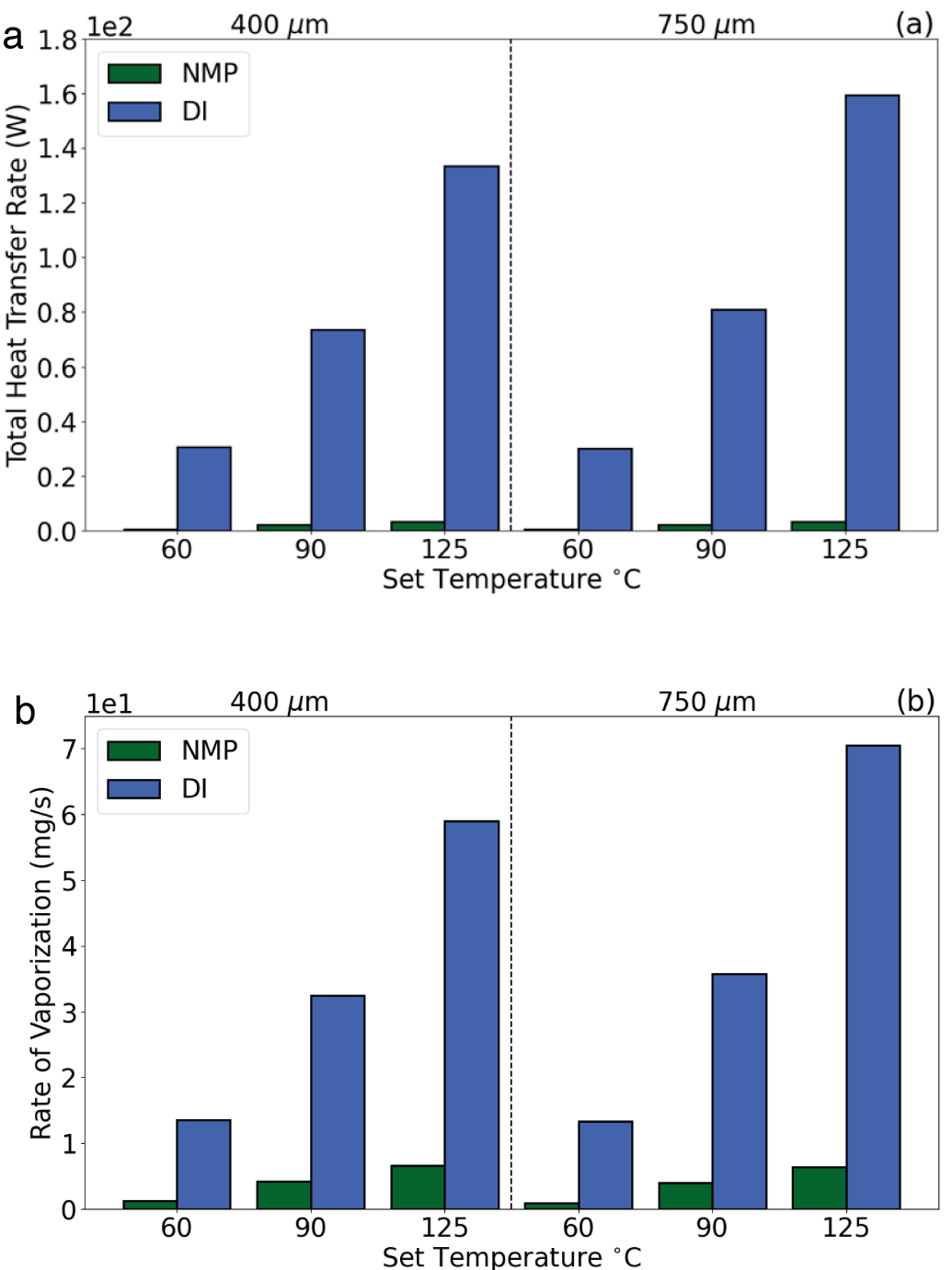


Figure 5. Total heat transfer rate to the a) NMP based electrode and b) DI based electrode ($-q$) and rate of vaporization (\dot{m}) for the c) NMP based electrode and d) DI based electrode.

be reduced by replacing NMP with DI water as the solvent of choice.^[28] The cost savings can be further increased when factoring in capital equipment costs. If the total time required to dry an electrode is lower, by analogue, a fixed speed roll-to-roll drying line would be shorter in length, thus reducing both machine cost and reducing the overall footprint required to produce electrodes. Although solid contents in this study were intentionally kept similar to provide similar benchmarks in

terms of amount of solvent removed, it is worth noting that the solid content can be much higher in aqueous dispersion.^[28]

Binder Distribution via ToF-SIMS

ToF-SIMS elemental maps are provided in Figure 6 for both DI and NMP processed samples. The binder distribution can be identified through the Cs_2F^{+} ion signal as the binders are the

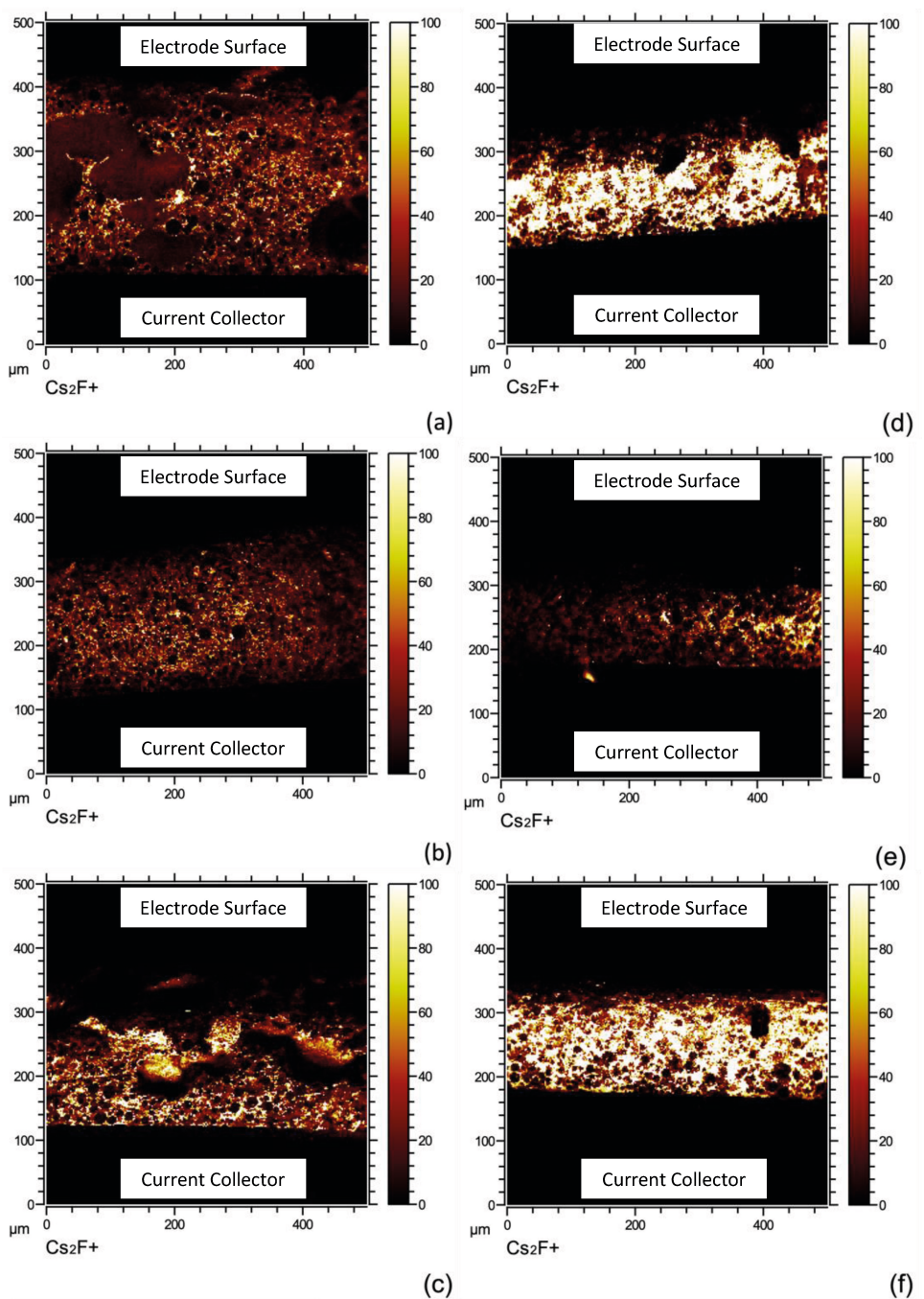


Figure 6. Elemental maps of fluorine distribution across the electrode cross-section for a) 60 °C DI, b) 90 °C DI, c) 125 °C DI, d) 60 °C NMP, e) 90 °C NMP, and f) 125 °C NMP 750 μm wet gap (6 mAh cm^{-2}) electrodes.

only fluorine source within the electrodes. For DI samples, the binder distribution is most homogenous at 90 °C, providing a potential explanation for increased electrochemical performance observed at high discharge rates, which is discussed in the next section. DI samples dried at 60 °C and 125 °C both exhibited inhomogeneous binder distributions with the 60 °C sample appearing to have pockets of increased binder concentration at random locations and the 125 °C sample having increased binder content near the current collector. It is difficult to ascribe the exact mechanism without being able to monitor

the development of the electrode during the drying process, but the poor binder distribution in the 60 °C DI based samples is most likely due to poor thermal distribution of the binder.

These effects are not though to be related to corrosion effects known to occur at the current collector interface because phosphoric acid was used in slurry preparation and has previously been shown to mitigate corrosive effects in aqueous processed nickel-rich active materials such as NMC 811.^[29] Furthermore, there is no evidence of void space in the chemical maps, which would be indicative of the gas generated via the

well-known corrosion reaction that takes place at the aluminum current collector.^[30] Similarly, as all electrodes were coated using the same slurry material, the differences in binder distribution cannot be attributed to differing mixing conditions and therefore must be driven by temperature differences alone. As the sedimentation potential of the active material should be relatively constant as the temperature differs, the most likely driver of the poor distribution is Brownian Thermal motion. The lowest investigated drying temperature likely was not sufficient to properly distribute the smaller polymer binder particles throughout the coating and resulted in regions of increased binder concentration. As the temperature is increased to 90 °C, the thermal motion is sufficient to promote proper binder distribution and thus a more homogenous binder signal is observed in Figure 6. However, as the temperature is further increased, the binder distribution is again negatively impacted, although in this scenario, increased capillary action as a result of a larger evaporation contribution is likely to blame.^[3,31]

NMP samples at each drying temperature display homogeneous binder distribution throughout the electrode suggesting the temperature range did not exceed the limit at which binder segregation in NMP processed electrodes begins and suggests a suitable binder distribution is attainable over a wide range of drying temperature for NMP based electrodes. These results also provide additional support to the earlier claim that NMP processed electrodes are less temperature sensitive as compared to their DI processed counterparts. This is beneficial from a processing standpoint as there exists a wider acceptable temperature range for processing, however this also means the overall energy input is not greatly impacted by drying temperature and thus savings will be minimal for NMP processed electrodes.

Electrochemical Testing

Rate capability results between solvents provide similar discharge capacities at almost all discharge rates as seen in Figure 7 are comparable to previous reports of both aqueous processed and ultra-thick electrodes.^[17a,32] For electrodes with 2.5 mAh/cm² areal loadings (400 µm), the NMP processed cells display a consistently higher discharge capacity, especially as discharge rates exceed 1 C. This is partially ascribed to the addition of phosphoric acid, which could form a non-conductive layer of Li₃PO₄ on NMC811 particles and results in higher charge transfer resistance.^[29] It is demonstrated that a moderate drying temperature (90 °C) produced electrodes with best rate performance regardless solvent selection and areal loading. These differences were most notable for samples produced with DI as the solvent. The specific discharge capacity at 1 C increased from 110 mAh/g to over 160 mAh/g for the 2.5 mAh/cm² DI coating when the drying temperature was increased from 60 °C to 90 °C as seen in Figure 7a. Other temperature driven differences in discharge capacity can also be identified such as the overall increase in discharge capacity for NMP processed electrodes at 90 °C. This difference is thought to be a result of the superior binder distribution of the 90 °C NMP

electrode as the electrochemical benefit is rather small, in line with the difference in binder distribution for the NMP samples. Although the sample appears to have increased binder homogeneity, the degree to which the distribution is improved is small. This result does suggest a universal ideal drying temperature of 90 °C, regardless of solvent choice. Naturally this may not be the ideal temperature but is the best performing drying temperature investigated in this study.

Differences in discharge capacity are also heavily impacted by the areal loading of the electrode as shown in Figure 7. Unsurprisingly, as the areal loading is more than doubled from 2.5 mAh/cm² to 6 mAh/cm², the discharge capacity decreases precipitously. This large decrease is due to mass transport limitations due to constrictive lithium-ion diffusion pathways within the electrode. Compounding this constrictive pore network, is the poor binder distribution previously identified by ToF-SIMS chemical mapping. Although the polymer binder does not participate in the electrochemical reaction directly, it facilitates the reaction by creating a conductive network of carbon black and active material particles. The effects of the poor binder distribution are the same as in the lower areal loading (2.5 mAh/cm²) cells, but the decrease in specific discharge capacity is much more pronounced in the higher areal loading cells.

It can be inferred from the electrochemical data that there is the detrimental effect of non-uniform binder distribution on cycling performance, a well-established trend. Less obvious is the connection to efficiency and cost savings. As aqueous processing continues to gain momentum for economic and environmental concerns, the identification of a preferred drying condition for such cathodes can lead to overall improvement in cycling performance. Demonstrated at all areal loadings for DI samples is a strong dependence on initial drying temperature. As most of the damage to electrode formation occurs during the initial film shrinkage stage of drying, tuning the initial drying temperature has the potential to result in radically different electrochemical performance for aqueous processed cathodes.

Conclusions

Aqueous processing of LIB cathodes was investigated via an in-depth chemical engineering model and electrochemical testing. The energy input required for DI samples was less than that of NMP samples and was more sensitive to changes in drying temperature than NMP samples as well. This suggests that DI samples could be initially dried at a temperature that maximizes the binder distribution homogeneity, here found to be 90 °C, and then the drying temperature could be increased to maximize the efficiency of the pore emptying stage. This combination would reduce the drying time and energy input considerably compared to current NMP processing. Binder distribution information gathered via ToF-SIMS confirms the optimal drying temperature for DI samples at 90 °C and confirms NMP samples are generally less sensitive to changes in drying temperature, provided the temperature is below the

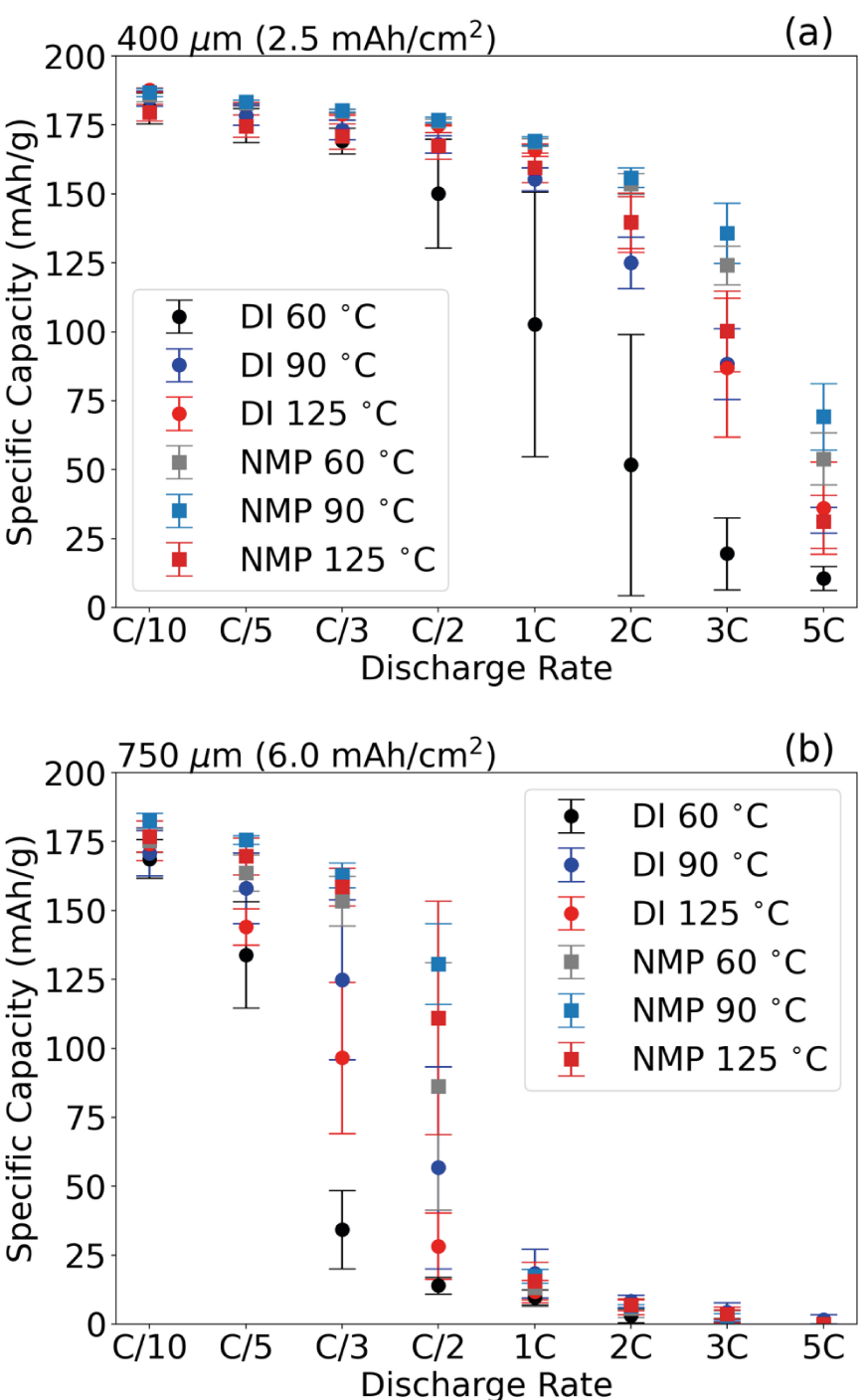


Figure 7. Rate capability results for a) 400 μm and b) 750 μm wet gaps at each drying temperature.

limit of binder migration occurring, which was not observed in this study for NMP samples. Electrochemically, the differences in cycling between NMP based samples was minimal while the DI samples exhibited a wide range of capacity with 90 °C again being the optimum, which is likely a result of the more homogenous binder distribution observed at this temperature and suggests tuning of drying temperature for aqueous processed cathodes is of great importance to electrochemical performance. Notably, the rate capability of the DI-processed

cathodes was lower than that of the NMP-based cathodes, suggesting more efforts are needed for the industrialization of aqueous processing of cathodes. Overall evidence is provided that DI-processed cathodes can be effectively produced and can provide an economic benefit to the LIB manufacturing.

Author Contributions

Alexander Kukay: Methodology, Investigation, Data curation, Visualization, Writing - original draft. Georgios Polizos: Data curation, Writing - review & editing. Emily Bott: Methodology, Data curation. Anton levlev: Investigation. Runming Tao: Writing - review & editing. Jaswinder Sharma: Visualization. Jianlin Li: Supervision, Funding acquisition, Conceptualization, Data curation, Writing - review & editing.

Acknowledgements

This research at Oak Ridge National Laboratory (ORNL), managed by UT Battelle, LLC, for the U.S. Department of Energy (DOE) under contract DE-AC05-00OR22725. The SEM and ToF-SIMS characterizations were performed at the Center for Nanophase Materials Sciences (CNMS) at ORNL, which is a DOE Office of Science User Facility. The authors wish to thank Chance Parrish and P. Randall Schunk of Sandia National Laboratory for their assistance in developing the initial model for this work.

Conflict of Interests

The authors declare no conflict of interest.

Data Availability Statement

The data that support the findings of this study are available from the corresponding author upon reasonable request.

Keywords: binder migration · heating · cathodes · lithium-ion battery · processing and manufacturing

- [1] a) J. B. Goodenough, *Nat. Electron.* **2018**, *1*, 204; b) J. Li, Y. Lu, T. Yang, D. Ge, D. L. Wood, Z. Li, *iScience* **2020**, *23*, 101081.
- [2] a) R. Tao, T. Zhang, S. Tan, C. J. Jafta, C. Li, J. Liang, X.-G. Sun, T. Wang, J. Fan, Z. Lu, C. A. Bridges, X. Suo, C.-L. Do-Thanh, S. Dai, *Adv. Energy Mater.* **2022**, *12*, 2200519; b) R. Tao, G. Yang, E. C. Self, J. Liang, J. R. Dunlap, S. Men, C.-L. Do-Thanh, J. Liu, Y. Zhang, S. Zhao, H. Lyu, A. P. Sokolov, J. Nanda, X.-G. Sun, S. Dai, *Small* **2020**, *16*, 2001884; c) R. Tao, T. Zhang, X.-G. Sun, C.-L. Do-Thanh, S. Dai, *Batteries & Supercaps* **2023**, *6*, e202300101; d) R. Tao, B. Steinhoff, C. H. Sawicki, J. Sharma, K. Sardo, A. Bishtawi, T. Gibbs, J. Li, *J. Power Sources* **2023**, *580*, 233379; e) R. Tao, Y. Gu, J. Sharma, K. Hong, J. Li, *Mater. Today Chem.* **2023**, *32*, 101672.
- [3] Y. S. Zhang, N. E. Courtier, Z. Zhang, K. Liu, J. J. Bailey, A. M. Boyce, G. Richardson, P. R. Shearing, E. Kendrick, D. J. L. Brett, *Adv. Energy Mater.* **2022**, *12*, 2102233.
- [4] a) Y. Liu, R. Zhang, J. Wang, Y. Wang, *iScience* **2021**, *24*, 102332; b) R. Tao, B. Steinhoff, X.-G. Sun, K. Sardo, B. Skelly, H. M. Meyer, C. Sawicki, G. Polizos, X. Lyu, Z. Du, J. Yang, K. Hong, J. Li, *Chem. Eng. J.* **2023**, *471*, 144300; c) R. Tao, B. Steinhoff, K. Uzun, B. La Riviere, K. Sardo, B. Skelly, R. Hill, Y.-T. Cheng, J. Li, *J. Power Sources* **2023**, *581*, 233481.
- [5] M. Zackrisson, L. Avellán, J. Orlenius, *J. Cleaner Prod.* **2010**, *18*, 1519.
- [6] a) D. L. Wood, J. Li, C. Daniel, *J. Power Sources* **2015**, *275*, 234; b) C.-C. Li, Y.-W. Wang, *J. Electrochem. Soc.* **2011**, *158*, A1361; c) R. Tao, S. Tan, H. M. Meyer III, X.-G. Sun, B. Steinhoff, K. Sardo, A. Bishtawi, T. Gibbs, J. Li, *ACS Appl. Mater. Interfaces* **2023**, *15*, 40488.
- [7] L. A.-W. Ellingsen, G. Majean-Bettez, B. Singh, A. K. Srivastava, L. O. Valøen, A. H. Strømman, *J. Ind. Ecol.* **2014**, *18*, 113.
- [8] a) P. E. Price Jr, I. H. Romdhane, *AIChE J.* **2003**, *49*, 309; b) C. Parrish, N. Bell, M. E. Larsen, K. Tjiptowidjojo, P. R. Schunk, *AIChE J.* **2023**, *69*, e18147.
- [9] a) S. Jaiser, M. Müller, M. Baunach, W. Bauer, P. Scharfer, W. Schabel, *J. Power Sources* **2016**, *318*, 210; b) S. Jaiser, N. Sanchez Salach, M. Baunach, P. Scharfer, W. Schabel, *Drying Technol.* **2017**, *35*, 1807; c) M. Stein, A. Mistry, P. P. Mukherjee, *J. Electrochem. Soc.* **2017**, *164*, A1616.
- [10] C. M. Cardinal, Y. D. Jung, K. H. Ahn, L. F. Francis, *AIChE J.* **2010**, *56*, 2769.
- [11] a) W. B. Hawley, J. Li, *J. Energy Storage* **2019**, *26*, 100994; b) W. Bauer, F. A. Çetinel, M. Müller, U. Kaufmann, *Electrochim. Acta* **2019**, *317*, 112; c) W. Bauer, D. Nötzel, *Ceram. Int.* **2014**, *40*, 4591; d) K. M. Kim, W. S. Jeon, I. J. Chung, S. H. Chang, *J. Power Sources* **1999**, *83*, 108; e) G.-W. Lee, J. H. Ryu, W. Han, K. H. Ahn, S. M. Oh, *J. Power Sources* **2010**, *195*, 6049; f) M. Wang, D. Dang, A. Meyer, R. Arsenault, Y.-T. Cheng, *J. Electrochem. Soc.* **2020**, *167*, 100518.
- [12] F. Font, B. Protas, G. Richardson, J. M. Foster, *J. Power Sources* **2018**, *393*, 177.
- [13] S. Jaiser, J. Kumberg, J. Klaver, J. L. Urai, W. Schabel, J. Schmatz, P. Scharfer, *J. Power Sources* **2017**, *345*, 97.
- [14] J. Li, Z. Du, R. E. Ruther, S. J. An, L. A. David, K. Hays, M. Wood, N. D. Phillip, Y. Sheng, C. Mao, S. Kalnaus, C. Daniel, D. L. Wood, *JOM* **2017**, *69*, 1484.
- [15] D. L. Wood, J. D. Quass, J. Li, S. Ahmed, D. Ventola, C. Daniel, *Drying Technol.* **2018**, *36*, 234.
- [16] Y. Bai, W. B. Hawley, C. J. Jafta, N. Muralidharan, B. J. Polzin, I. Belharouak, *Sustain. Mater. Technol.* **2020**, *25*, e00202.
- [17] a) A. Kukay, R. Sahore, A. Parejiya, W. Blake Hawley, J. Li, D. L. Wood, *J. Colloid Interface Sci.* **2021**, *581*, 635; b) M. Wood, J. Li, R. E. Ruther, Z. Du, E. C. Self, H. M. Meyer, C. Daniel, I. Belharouak, D. L. Wood, *Energy Storage Mater.* **2020**, *24*, 188.
- [18] a) I. Doberdò, N. Löfller, N. Laszcynski, D. Cericola, N. Penazzi, S. Bodoardo, G.-T. Kim, S. Passerini, *J. Power Sources* **2014**, *248*, 1000; b) W. B. Hawley, H. M. Meyer, J. Li, *Electrochim. Acta* **2021**, *380*, 138203; c) W. B. Hawley, A. Parejiya, Y. Bai, H. M. Meyer, D. L. Wood, J. Li, *J. Power Sources* **2020**, *466*, 228315; d) R. Sahore, D. L. Wood, III, A. Kukay, K. M. Grady, J. Li, I. Belharouak, *ACS Sustainable Chem. Eng.* **2020**, *8*, 3162.
- [19] P. Kneisl, J. W. Zondlo, *J. Chem. Eng. Data* **1987**, *32*, 11.
- [20] J. Li, J. Fleetwood, W. B. Hawley, W. Kays, *Chem. Rev.* **2022**, *122*, 903.
- [21] M. Müller, L. Pfaffmann, S. Jaiser, M. Baunach, V. Trouillet, F. Scheiba, P. Scharfer, W. Schabel, W. Bauer, *J. Power Sources* **2017**, *340*, 1.
- [22] M. Baunach, S. Jaiser, S. Schmelzle, H. Nirschl, P. Scharfer, W. Schabel, *Drying Technol.* **2016**, *34*, 462.
- [23] M. M. Forouzan, C.-W. Chao, D. Bustamante, B. A. Mazzeo, D. R. Wheeler, *J. Power Sources* **2016**, *312*, 172.
- [24] H. Hagiwara, W. J. Suszynski, L. F. Francis, *J. Coat. Technol. Res.* **2014**, *11*, 11.
- [25] T. L. Bergman, *Fundamentals of Heat and Mass Transfer*, John Wiley & Sons, 2011.
- [26] T. H. Chilton, A. P. Colburn, *Ind. Eng. Chem.* **1934**, *26*, 1183.
- [27] N. Susarla, S. Ahmed, D. W. Dees, *J. Power Sources* **2018**, *378*, 660.
- [28] D. L. Wood III, M. Wood, J. Li, Z. Du, R. E. Ruther, K. A. Hays, N. Muralidharan, L. Geng, C. Mao, I. Belharouak, *Energy Storage Mater.* **2020**, *29*, 254.
- [29] N. Loeffler, G.-T. Kim, F. Mueller, T. Diermant, J.-K. Kim, R. J. Behm, S. Passerini, *ChemSusChem* **2016**, *9*, 1112.
- [30] a) L. Neidhart, K. Fröhlich, N. Eshraghi, D. Cupid, F. Winter, M. Jahn, *Nanomaterials* **2022**, *12*, 317; b) B. C. Church, D. T. Kaminski, J. Jiang, *J. Mater. Sci.* **2014**, *49*, 3234.
- [31] Y. S. Zhang, A. N. P. Radhakrishnan, J. B. Robinson, R. E. Owen, T. G. Trantter, E. Kendrick, P. R. Shearing, D. J. L. Brett, *ACS Appl. Mater. Interfaces* **2021**, *13*, 36605.
- [32] A. Heist, S.-H. Lee, *J. Electrochem. Soc.* **2019**, *166*, A1860.

Manuscript received: February 21, 2024

Revised manuscript received: April 27, 2024

Accepted manuscript online: April 28, 2024

Version of record online: June 11, 2024